X-IGALME: Isogeometric analysis extended with local maximum entropy for fracture analysis

Farshid Fathi | Lin Chen | René de Borst*

Department of Civil and Structural
Engineering, University of Sheffield,
Sheffield, UK

Correspondence
*Department of Civil and Structural
Engineering, University of Sheffield,
Sheffield, S1 3JD, UK
Email: r.deborst@sheffield.ac.uk

ABSTRACT

An extended approach is developed by blending isogeometric analysis and the first-order local maximum entropy for the standard and the enhanced fields, respectively. Isogeometric analysis facilitates the accurate parametrisation of the geometry in general, particularly the exact geometric parametrisation of the conic curves and quadratic surfaces using NURBS. On the other hand, the local maximum entropy leads to an improved estimate for the enhanced part due to its infinite continuity. Moreover, local maximum entropy paves the way to a non-elementwise crack propagation owing to its meshfree characteristic. To enforce compatibility, the shifting technique is amended for the meshfree enhanced part to localise the effect of the Heaviside function to a narrow region around the crack. Next, a blending technique is exploited to remove the effect of the discontinuity in front of the crack tip. The viability of the approach is illustrated at the hand of several examples comprising straight and curved crack propagation.

KEYWORDS:
Extended finite element method, isogeometric analysis, meshless method, local maximum entropy, cohesive fracture

1 | INTRODUCTION

The classical approach to simulate discrete fracture is the use of interface elements [1,2,3,4]. The method is suitable and straightforward when the crack path is known *a priori*. For arbitrary crack paths the method is more cumbersome, as advanced remeshing schemes have to be used, but successful applications have been reported, in the context of Linear Elastic Fracture Mechanics (LEFM) [5] as well as for cohesive fracture [6].

The eXtended Finite Element Method (XFEM) offers an elegant alternative and can capture an arbitrary-shaped discontinuity independent of the original mesh layout by exploiting the partition of unity property of the shape functions. The approach utilises an additional set of discontinuous functions with extra degrees of freedom, potentially different from the regular degrees of freedom, and discontinuities can run through elements. As for remeshing, the method has been developed for Linear Elastic Fracture Mechanics [7,8,9] as well as for cohesive fracture [10,11]. It is finally noted that the method can be considered as a generalisation of interface elements, where discontinuity is put at the edge of elements rather than inside.

The finite element normally uses Lagrange shape functions, which leads to a C^0-continuity across element boundaries. To provide a higher-continuity across element boundaries and, especially, to capture the geometry exactly, Lagrange interpolation functions have been replaced by Non-Uniform Rational B-Splines (NURBS), and the resulting method has been named Isogeometric Analysis (IGA) [12]. Unfortunately, the tensor-product structure of NURBS makes them not very suitable for the simulation

of discrete crack propagation. There are several solutions, including the use of T-splines [13,14], splines which are based on triangles, so-called Powell-Sabin B-Splines [15,16] and an approach which is similar to that of XFEM and exploits the partition-of-unity property of NURBS. This method has been coined eXtended Isogeometric Analysis (XIGA). It was originally proposed by De Luycker *et al.* [17] for Linear Elastic Fracture Mechanics. Recently, the approach has been developed for cohesive fracture [18] and has been extended to geometric nonlinearity [19].

Maximum entropy (*max-ent*) – a principle to obtain the least biased statistical inference in the absence of sufficient knowledge – is a means to find the current state of an ensemble whose probabilities form a partition of unity [20]. Applications encompass diverse fields, including engineering, where it has been used to obtain the minimally biased interpolation on a polygonal domain [20,21], among other applications. To localise the support of *max-ent* basis functions *Local* Maximum Entropy (LME) has been developed [22]. First-order LME approximants are non-negative on a convex hull of the ensemble, while for the extension to a higher-order approximants the non-negativity assumption is generally dropped [23]. Nevertheless, positivity and smoothness of the basis functions can be preserved for higher-order approximants, for instance within a second-order convex maximum entropy approach [24].

Among meshfree approaches *max-ent* holds some superior features, including positivity of the basis functions, robustness of the solution, a straightforward quadrature rule, and a weak Kronecker-delta property at boundaries, which facilitates the imposition of essential boundary conditions [22,25]. The meshfree shape functions are unbounded, forming a local support around the point under consideration. This locality is adjustable through a parameter to control the size of the support [22,25,26]. Therefore, the supports of the basis functions overlap, similar to isogeometric analysis.

As with other meshfree approaches, the main drawback is the poor approximation of complex boundaries. This has been solved by incorporating Isogeometric Analysis (IGA), e.g. by coupling IGA with the Reproducing Kernel Particle Method (RKPM) [27] and with *max-ent*-based approximants via a duality method [21]. From the computational cost perspective, meshfree approaches such as RKPM and EFG are less costly compared to LME, since they only solve a linear system of equations instead of a nonlinear problem. Recently, the LME strategy has been improved by anisotropy in the basis function support to account for directional variations in nodal spacing, and a remedy for the tensile instability observed in most meshfree approaches [28]. In the realm of Linear Elastic Fracture Mechanics, Local Maximum Entropy has been cast in the extended framework (XLME) for the standard and the enhanced sections [29]. XLME, indeed, improves the performance compared to XFEM, which is proven for different errors benchmarked against well-established LEFM problems. Compatibility enforcement [30,17], however, has not been considered for XLME to confine the effect of the enhanced field perpendicular and parallel to the crack path [17,18]. Moreover, while all the examples are merely limited to straight fracture with no propagation, the efficacy of this approach on arbitrary crack propagation in an iterative nonlinear problem is interesting to explore.

Herein, we aim to exploit IGA and LME in an extended approach, where the former is the standard part which represents the geometry exactly and the latter captures the localised high gradient which results from the discontinuity. Similar to the higher-order continuity C^p $p > 1$ provided by isogeometric analysis, smoothness of basis functions is an advantages of meshfree methods In particular, *max-ent* returns C^∞-continuity which is better than in isogeometric analysis [25]. This, for instance, can be exploited when solving higher-order differential equations, e.g. the Cahn-Hilliard equation [31,32]. Recent research on XIGA for cohesive fracture and the difficulties encountered for element-wise enrichment of the individual control points with higher-order continuities [18] have motivated this blending, coined X-IGALME. By setting LME as the enhanced part in the extended approach, an improved stress estimation and consequently, a better crack propagation direction is expected. This complements the improved estimation of the crack extension direction by the standard IGA part due to its higher-order inter-element continuity.

This contribution starts with a succinct discussion of the governing equations in the bulk and at the discontinuity. The IGA and LME formulations are presented for the standard and the enhanced parts as the main ingredients for X-IGALME. Next, implementation aspects, which encompass compatibility, enrichment and crack extension, are covered. The paper concludes with some case studies, which assess the NURBS order and the effect of the dimensionless aspect ratio on the energy dissipation for straight and curved crack profiles.

2 | GOVERNING EQUATIONS

We adopt rate-independent, isotropic linear elasticity for the bulk, while a cohesive-zone model governs the behaviour at the discontinuity, see Figure 1.
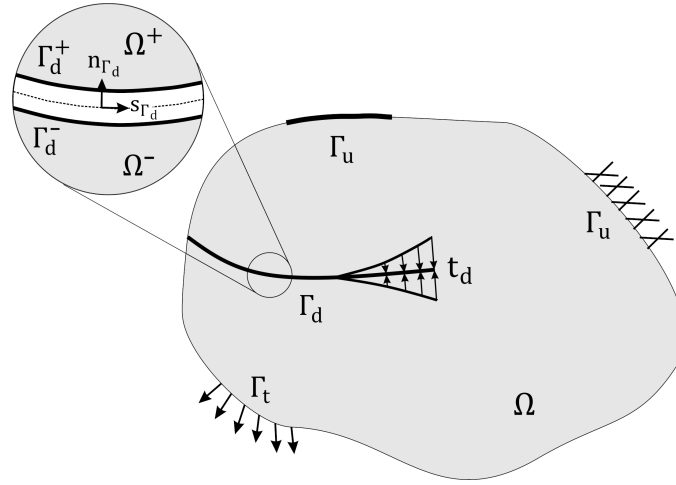
FIGURE 1 Boundary value problem Ω with the discontinuity Γ_d and cohesive tractions $\mathbf{t}_d$.

2.1 | Cohesive-zone model

An exponentially decaying function governs the relation between the local tractions normal to the discontinuity and the relative opening:

$$t_n^{\text{loc}} = f_t \exp\left(-\frac{f_t}{G_f}\kappa\right) \tag{1}$$

where κ denotes a history parameter. f_t and G_f indicate the fracture strength and the fracture energy, respectively. Using the rotation matrix this relation can be transformed from local to global coordinate system and can subsequently belinearised for use in a Newton-Raphson iterative scheme. To obtain a symmetric stiffness matrix, the shear stiffness must be neglected, which holds true for mode-I dominated fracture problems, which is the case in all the examples. Kuhn-Tucker conditions govern loading/unloading behaviour:

$$f\left(\llbracket u_n \rrbracket, \kappa\right) = \llbracket u_n \rrbracket - \kappa \leq 0 \quad \dot{\kappa} \geq 0 \quad \dot{\kappa} f = 0 \tag{2}$$

where $\llbracket u_n \rrbracket$ is the displacement jump normal to the crack.

2.2 | Kinematics of displacement discontinuity

In the absence of acceleration and body forces, the equilibrium equation and the boundary conditions read (see Figure 1):

$$\begin{cases} \nabla \cdot \boldsymbol{\sigma} = 0 & \mathbf{x} \in \Omega \\ \mathbf{u} = \bar{\mathbf{u}} & \mathbf{x} \in \Gamma_u \\ \mathbf{n} \cdot \boldsymbol{\sigma} = \bar{\mathbf{t}} & \mathbf{x} \in \Gamma_t \\ \mathbf{n}_{\Gamma_d} \cdot \boldsymbol{\sigma} = \mathbf{t}_d & \mathbf{x} \in \Gamma_d \end{cases} \tag{3}$$

where $\boldsymbol{\sigma}$ is the Cauchy stress tensor, and $\bar{\mathbf{u}}$ and $\bar{\mathbf{t}}$ are the prescribed displacement and traction, respectively. The vector normal to the external traction surface is defined as $\mathbf{n}$, and $\mathbf{n}_{\Gamma_d}$ denotes the vector normal to the crack surface. The linear-elastic stress-strain relation for the bulk material is:

$$\boldsymbol{\sigma} = \mathbf{D} : \boldsymbol{\epsilon} \tag{4}$$

where $\mathbf{D}$ is the fourth-order linear-elastic stiffness tensor.

In an Extended Finite Element Approach the displacement field is separated into regular and (possibly multiple) enhanced fields[7,8,10,11,9,18]. It is noted that the partition of unity property of interpolation functions is the requirement for this separation, and also applies to shape functions used in meshless methods and in isogeometric analysis. The regular degrees of freedom $\mathbf{a}$ represent the regular continuous displacement field, and the enhanced degrees of freedom $\mathbf{b}$ are used for the parameterisation of the additional displacement field:

$$\mathbf{u}(\mathbf{x}) = \mathbf{N}(\mathbf{x})\mathbf{a} + \mathcal{H}_{\Gamma_d}(\mathbf{x})\tilde{\mathbf{N}}(\mathbf{x})\mathbf{b} \tag{5}$$

where $\mathbf{N}$ and $\tilde{\mathbf{N}}$ contain the basis functions of the standard and the enhanced fields, respectively. $\mathcal{H}_{\Gamma_d}$ is the enrichment function which determines the character of the discontinuity. Herein, a sign function is utilised for modelling the crack as a strong discontinuity [18]. Assuming small strains, the symmetrised gradient of Equation (5) reads:

$$\boldsymbol{\epsilon} = \mathbf{Ba} + \mathcal{H}_{\Gamma_d}\tilde{\mathbf{B}}\mathbf{b} + 2\left(\delta_{\Gamma_d}\mathbb{n}_{\Gamma_d}\right)\tilde{\mathbf{N}}\mathbf{b} \tag{6}$$

where $\mathbf{B}$ and $\tilde{\mathbf{B}}$ are the matrices which contain the derivatives of the set of basis functions $\mathbf{N}$ and $\tilde{\mathbf{N}}$, respectively. δ_{Γ_d} is the Dirac delta function and $\mathbb{n}_{\Gamma_d}$ contains components of $\mathbf{n}_{\Gamma_d}$ [18].

3 | X-IGALME

Both IGA and LME form a partition of unity, which is required within an extended approach to employ multiple fields. Also, they both maintain higher continuity, although in a different manner. While this term usually denotes the presence of an higher inter-element continuity in IGA, it is defined locally in LME since the notion of an element is meaningless in a meshless approach. Therefore, the terminology "higher order" denotes the C^∞-continuity for the ensemble, or more precisely, for the support cloud of the nominated local point. This provides a potential for higher accuracy compared to finite element approaches, including IGA. Noteworthy is that the higher accuracy results is assured for smooth problems [22], while it is yet to be confirmed for non-smooth problems. The localisation parameter to control the width of the meshfree basis functions also provides a more versatile approach to enforce compatibility, which is of paramount importance for enriched approaches in returning the correct solution and/or optimum convergence [18,19].
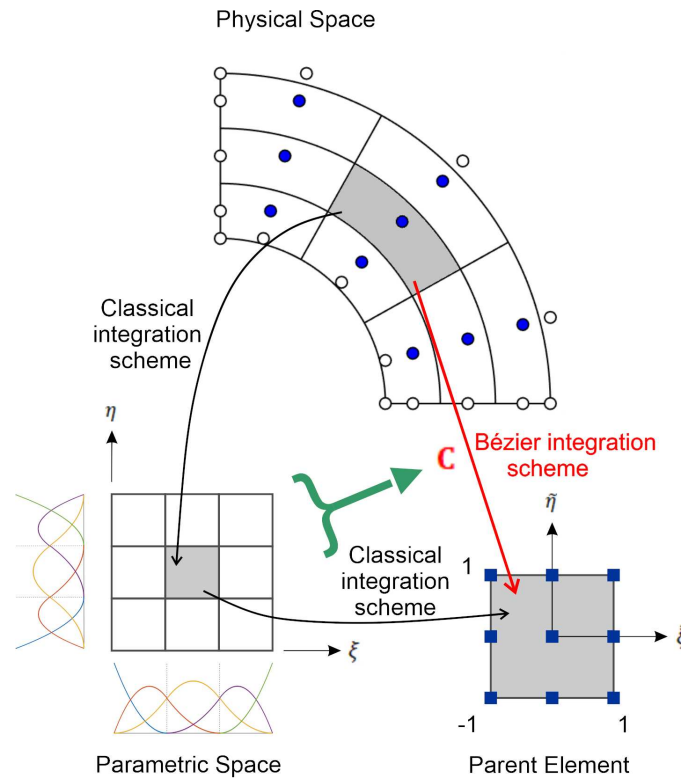
FIGURE 2 Bézier extraction-based integration scheme which directly maps the physical domain and the parent element, identical to standard finite element procedures. This scheme is compared with the classical integration scheme involving two mappings. Note that $\mathbf{C}$ is the Bézier extraction operator which contains information of the parametric domain. Circles denote the control points and squares show the elements.

3.1 | NURBS for the standard section

We now briefly review NURBS using Bézier extraction. NURBS basis functions, i.e. weighted B-spline basis functions, can accurately parametrise conic shapes, a characteristic which has led to the use of NURBS in state-of-the-art Computer Aided Design. The geometry can be written as a linear combination of the NURBS basis functions $R_k(\xi)$, which map a parametric coordinate ξ onto the physical domain:

$$\mathbf{x}(\xi) = \sum_{k=1}^{n_{\text{IGA}}} R_k(\xi)\mathbf{P}_k \tag{7}$$

where $\mathbf{P}$ is the set of control point coordinates and n_{IGA} is the number of control points. The weight w_k makes the difference between a B-spline basis function N_k and a NURBS basis function:

$$R_{k,p}(\xi) = \frac{w_k N_{k,p}}{W(\xi)} \tag{8}$$

with p denoting the order of the underlying knot vector and $W(\xi) = \sum_{k=1}^{n} N_k(\xi)w_k$. B-spline basis functions are recursively defined by the Cox-de Boor formula[33]. To provide an element-wise framework in compliance with standard finite element data structures, Bézier extraction has been exploited[34,35]. This facilitates the numerical integration, which is illustrated in Figure 2. The element-wise NURBS basis functions are defined as:

$$\mathbf{R}^e(\boldsymbol{\xi}) = \mathbf{W}^e \mathbf{C}^e \frac{\boldsymbol{\mathcal{B}}^e(\boldsymbol{\xi})}{W^e(\boldsymbol{\xi})} \tag{9}$$

where $\mathbf{W}^e$ is the diagonal matrix of weights, $\boldsymbol{\mathcal{B}}^e$ is the set of basis functions containing Bernstein polynomials, and $\mathbf{C}^e$ is the Bézier extraction operator[18].
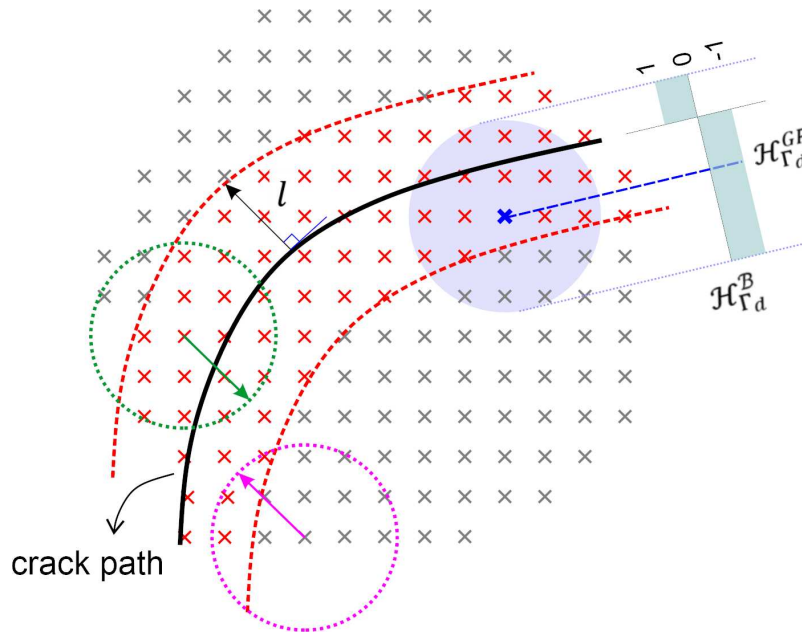
FIGURE 3 Compatibility enforcement via the shifting technique. Enriched points are indicated by red crosses, bounded by l-distanced offsets from the crack profile (see the dashed red lines). This region identifies those points with a support which intersects the crack path, i.e. comparing the dashed green circle with the magenta circle (both radius equals l). To represent the shifting technique, the values of the Heaviside function are illustrated for the blue point and its support (the purple shade). It is noted that $\mathcal{H}_{\Gamma_d}^{B}$ and $\mathcal{H}_{\Gamma_d}^{GP}$ denote the Heaviside value for control points and the nominated Gauss point, respectively.
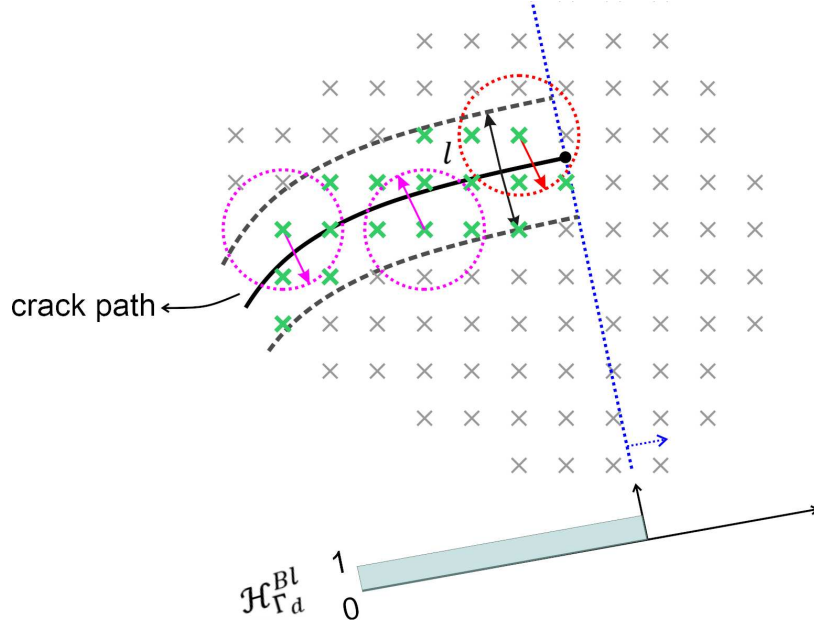
FIGURE 4 Compatibility enforcement via blending technique to impede the effect of enrichment in front of the crack tip (the black knot). Enrichment is also affected: points before the dashed blue line (the border between positive and negative tangential distance with respect to the crack tip) are enriched, which are indicated by green crosses. The blending Heaviside function acts like a weight function which removes the support excess of an enriched point with respect to the dashed blue line, e.g. the red dashed circle. The magenta dashed circles are completely inside the zone where $\mathcal{H}_{\Gamma_d}^{Bl} = 1$.

3.2 │ LME for the enhanced section

We consider an ensemble $\mathbb{X}$ as a subset of $\mathbb{R}^d$, with d is the dimension of the ensemble, so that the convex hull of the node set reads[21],

$$\text{conv}\mathbb{X} = \left\{ \mathbf{x} \in \mathbb{R}^d \mid \mathbf{x} = \sum_{l=1}^{n_{\text{LME}}} q_l \mathbf{x}_l, \sum_{l=1}^{n_{\text{LME}}} q_l = 1, q_l \geq 0 \right\} \tag{10}$$

where n_{LME} is the number of control points within the ensemble. The conditions in Equation (10) guarantee an exact approximation of an affine function[22]. Moreover, convexity is the requirement to maintain a weak Kronecker-delta property at the boundaries, which subsequently makes vanish the effect of internal bases at the boundary[21]. Therefore, similar to IGA, the geometry can be approximated as a linear combination of LME basis functions q_l:

$$\mathbf{x} = \sum_{l=1}^{n_{\text{LME}}} q_l(\mathbf{x})\mathbf{P}_l \tag{11}$$

where $\mathbf{P}_l$ is the same set of control points defined for IGA which has been already adopted as the node set $\mathbf{x}_l$ in Equation (10). LME basis function should form the zero-th and the first-order consistency conditions in an αth-order equation:

$$\sum_{l=1}^{n_{\text{LME}}} q_l(\mathbf{x})\mathbf{x}_l^{\alpha} = \mathbf{x}^{\alpha}, \quad \alpha = 0, 1. \tag{12}$$

The LME program can now be cast as a Pareto set, a platform to harmonise the unbiased estimation of *max-ent* and locality to control the width of basis functions[22]:

$$\text{LME}_{\beta} \quad \text{For fixed } \mathbf{x} \text{ minimise} \quad \sum_{l=1}^{n_{\text{LME}}} q_l \ln q_l + \sum_{l=1}^{n_{\text{LME}}} \beta_l q_l |\mathbf{x} - \mathbf{x}_l|^2$$

$$\text{subject to} \quad q_l \geq 0, \; l = 1, ..., n_{\text{LME}} \tag{13}$$

$$\mathbf{x} = \sum_{l=1}^{n_{\text{LME}}} q_l \mathbf{x}_l, \; \sum_{l=1}^{n_{\text{LME}}} q_l = 1$$

where β is a non-negative parameter weighing which objective overrules the other. It can be defined in terms of a dimensionless aspect ratio γ and the nodal spacing h as $\beta_l = \gamma_l/h_l^2$. The constraints subjected to the convex program guarantee non-negative

meshfree basis functions with C^∞-continuity[21]. Finally, the LME basis function reads[21,22,25],

$$q_l(\mathbf{x}) = \frac{1}{Z(\mathbf{x}, \boldsymbol{\lambda}^*)} \exp\left[-\beta_l |\mathbf{x} - \mathbf{x}_l|^2 + \boldsymbol{\lambda}^*(\mathbf{x}) \cdot (\mathbf{x} - \mathbf{x}_l)\right] \tag{14}$$

where

$$Z(\mathbf{x}, \boldsymbol{\lambda}) = \sum_{j=1}^{n_{\text{LME}}} \exp\left[-\beta_j |\mathbf{x} - \mathbf{x}_j|^2 + \boldsymbol{\lambda}(\mathbf{x}) \cdot (\mathbf{x} - \mathbf{x}_j)\right] \tag{15}$$

and

$$\boldsymbol{\lambda}^*(\mathbf{x}) = \arg \min_{\boldsymbol{\lambda} \in \mathbb{R}^d} \ln Z(\mathbf{x}, \boldsymbol{\lambda}). \tag{16}$$

3.3 | Finite element-meshfree discretisation

We now present the discretised governing equations. The weak form of Equation (3) reads:

$$\int_\Omega \nabla^s \delta\mathbf{u} : \boldsymbol{\sigma} \, d\Omega - \int_{\Gamma_u} \delta\mathbf{u} \cdot \bar{\mathbf{t}} \, d\Gamma = 0 \tag{17}$$

which must hold for all kinematically admissible variations $\delta\mathbf{u}$ and can be decomposed into the following weak forms, corresponding to the regular $\delta\hat{\mathbf{u}}$ and the enhanced $\delta\tilde{\mathbf{u}}$ displacement fields, respectively[18]:

$$\int_\Omega \nabla^s \delta\hat{\mathbf{u}} : \boldsymbol{\sigma} \, d\Omega = \int_{\Gamma_u} \delta\hat{\mathbf{u}} \cdot \bar{\mathbf{t}} \, d\Gamma \tag{18a}$$

$$\int_\Omega \mathcal{H}_{\Gamma_d}(\nabla^s \delta\tilde{\mathbf{u}}) : \boldsymbol{\sigma} \, d\Omega + 2\int_{\Gamma_d} \delta\tilde{\mathbf{u}} \cdot \mathbf{t}_d \, d\Gamma = \int_{\Gamma_u} \mathcal{H}_{\Gamma_d} \delta\tilde{\mathbf{u}} \cdot \bar{\mathbf{t}} \, d\Gamma. \tag{18b}$$

Considering Equations 5 and 6, and the NURBS and LME approximations in Sections 3.1 and 3.2, the discretised formulations become:

$$\int_\Omega \mathbf{B}_{\text{IGA}}^{\text{T}} \boldsymbol{\sigma} \, d\Omega = \int_{\Gamma_u} \mathbf{R}^{\text{T}} \bar{\mathbf{t}} \, d\Gamma \tag{19a}$$

$$\int_\Omega \mathcal{H}_{\Gamma_d} \mathbf{B}_{\text{LME}}^{\text{T}} \boldsymbol{\sigma} \, d\Omega + 2\int_{\Gamma_d} \mathbf{q}^{\text{T}} \mathbf{t}_d \, d\Gamma = \int_{\Gamma_u} \mathcal{H}_{\Gamma_d} \mathbf{q}^{\text{T}} \bar{\mathbf{t}} \, d\Gamma \tag{19b}$$

where it is recalled that $\mathbf{R}$ and $\mathbf{q}$ are the NURBS and LME basis functions, respectively. The linearised set of equations then reads:

$$\begin{bmatrix} \mathbf{K}_{\text{aa}} & \mathbf{K}_{\text{ab}} \\ \mathbf{K}_{\text{ab}} & \mathbf{K}_{\text{bb}} \end{bmatrix} \begin{bmatrix} \Delta\mathbf{a} \\ \Delta\mathbf{b} \end{bmatrix} = \begin{bmatrix} \mathbf{f}_{\text{a}}^{\text{ext}} \\ \mathbf{f}_{\text{b}}^{\text{ext}} \end{bmatrix} - \begin{bmatrix} \mathbf{f}_{\text{a}}^{\text{int}} \\ \mathbf{f}_{\text{b}}^{\text{int}} \end{bmatrix} \tag{20}$$

with the arrays

$$\mathbf{f}_{\text{a}}^{\text{ext}} = \int_{\Gamma_u} \mathbf{R}^{\text{T}} \bar{\mathbf{t}} \, d\Gamma \tag{21a}$$

$$\mathbf{f}_{\text{b}}^{\text{ext}} = \int_{\Gamma_u} \mathcal{H}_{\Gamma_d} \mathbf{q}^{\text{T}} \bar{\mathbf{t}} \, d\Gamma \tag{21b}$$

$$\mathbf{f}_{\text{a}}^{\text{int}} = \int_\Omega \mathbf{B}_{\text{IGA}}^{\text{T}} \boldsymbol{\sigma} \, d\Omega \tag{21c}$$

$$\mathbf{f}_{\text{b}}^{\text{int}} = \int_\Omega \mathcal{H}_{\Gamma_d} \mathbf{B}_{\text{LME}}^{\text{T}} \boldsymbol{\sigma} \, d\Omega + 2\int_{\Gamma_d} \mathbf{q}^{\text{T}} \mathbf{t}_d \, d\Gamma \tag{21d}$$

and the stiffness matrices:

$$\mathbf{K}_{\text{aa}} = \int_\Omega \mathbf{B}_{\text{IGA}}^{\text{T}} \mathbf{D} \mathbf{B}_{\text{IGA}} \, d\Omega \tag{22a}$$

$$\mathbf{K}_{ab} = \int_{\Omega} \mathcal{H}_{\Gamma_d} \mathbf{B}_{IGA}^T \mathbf{D} \mathbf{B}_{LME} \, d\Omega \tag{22b}$$

$$\mathbf{K}_{ba} = \int_{\Omega} \mathcal{H}_{\Gamma_d} \mathbf{B}_{LME}^T \mathbf{D} \mathbf{B}_{IGA} \, d\Omega \tag{22c}$$

$$\mathbf{K}_{bb} = \int_{\Omega} \mathbf{B}_{LME}^T \mathbf{D} \mathbf{B}_{LME} \, d\Omega + 4 \int_{\Gamma_d} \mathbf{q}^T \mathbf{Q}^T \mathbf{T}_d \mathbf{Q} \mathbf{q} \, d\Gamma. \tag{22d}$$

Herein, $\mathbf{Q}$ is the rotation matrix and $\mathbf{T}_d = \partial \mathbf{t}_d / \partial [\![\mathbf{u}]\!]$ is the linearised tangent stiffness of the traction-relative displacement relation. It is noted that, based on the Heaviside sign function, the displacement jump becomes $[\![\mathbf{u}]\!] = 2 \sum_{l=1}^{n_{enr}} q_l(\mathbf{x}) b_l$ [18], where n_{enr} is the number of enriched points.
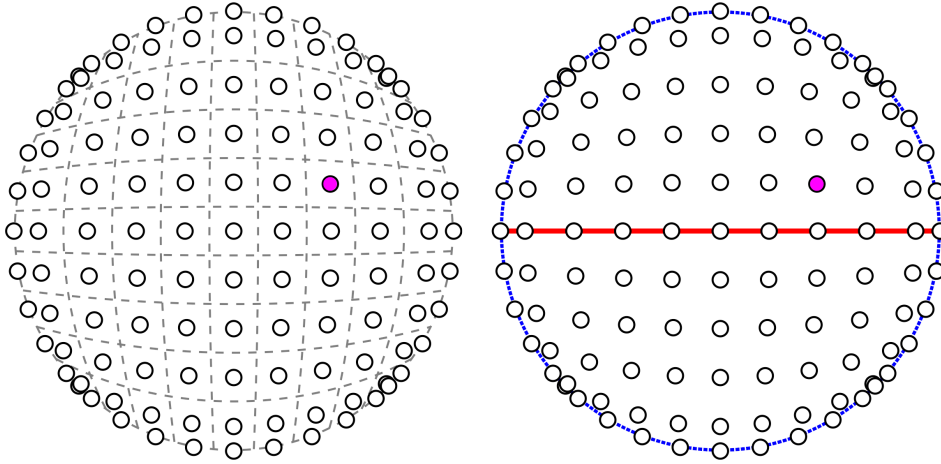
FIGURE 5 Disk with a unit radius. A quadratic IGA discretisation is chosen for the standard part (left), while the same node set of control points is utilised for the LME approach in the enhanced part (right). The crack is indicated by the red solid line. The magenta marker shows the location of the point for which the basis functions and the corresponding gradients have been plotted in Figure 6.

4 | IMPLEMENTATION ASPECTS

The extensive overlap in the supports of meshfree clouds impedes a straightforward enrichment of individual points during crack propagation. Also, employing an extended approach necessitates compatibility enforcement to localise the effect of the Heaviside function into a narrow region in the vicinity of the discontinuity (ideally removing the effect of the second function at the location of the control points). With overlapping basis functions, however, a complete removal is impossible. Therefore, compatibility enforcement narrows it down to a small region around the crack, reducing the error to a sufficiently small region [18]. Otherwise, all points within the enhanced field will be involved, increasing the computation error and a possible loss of optimal convergence [19].

4.1 | Enhancement of individual control points and the integration scheme

Within IGA the inter-element sharing of control points complicates the enrichment scheme [18]. Unlike IGA, however, the absence of the notion of an element within a meshless approach facilitates a more global definition of enrichment: points behind the crack tip whose supports intersect the crack path will be enriched. As illustration, the enrichment scheme for a uniform node set is shown in Figures 3 and 4. Points within the zone between l-distanced offsets from the crack path (see Figure 3) and before the crack tip (see Figure 4) are enriched, where $l = \sqrt{-\ln(\text{TOL}_0)/\gamma} h$ and TOL_0 is the tolerance for vanishing the support of the

LME basis function. The length l can be considered as a function of nodal spacing h and a scalar Λ, $l = \Lambda h$ (see Table 1). For smaller values of γ the support of the basis function becomes bigger, and consequently, the distribution of the basis becomes smoother[21]. For instance, $\gamma = 0.1$ returns a radius which approximately equals 9 times the nodal spacing h (considering a uniform node set).

Integration cells have been utilised within the LME approach[21]. Herein, the same IGA discretisation is used as the integration cells which is equipped with subtriangulation for cracked elements. Integration points are defined using a standard Gaussian quadrature rule.
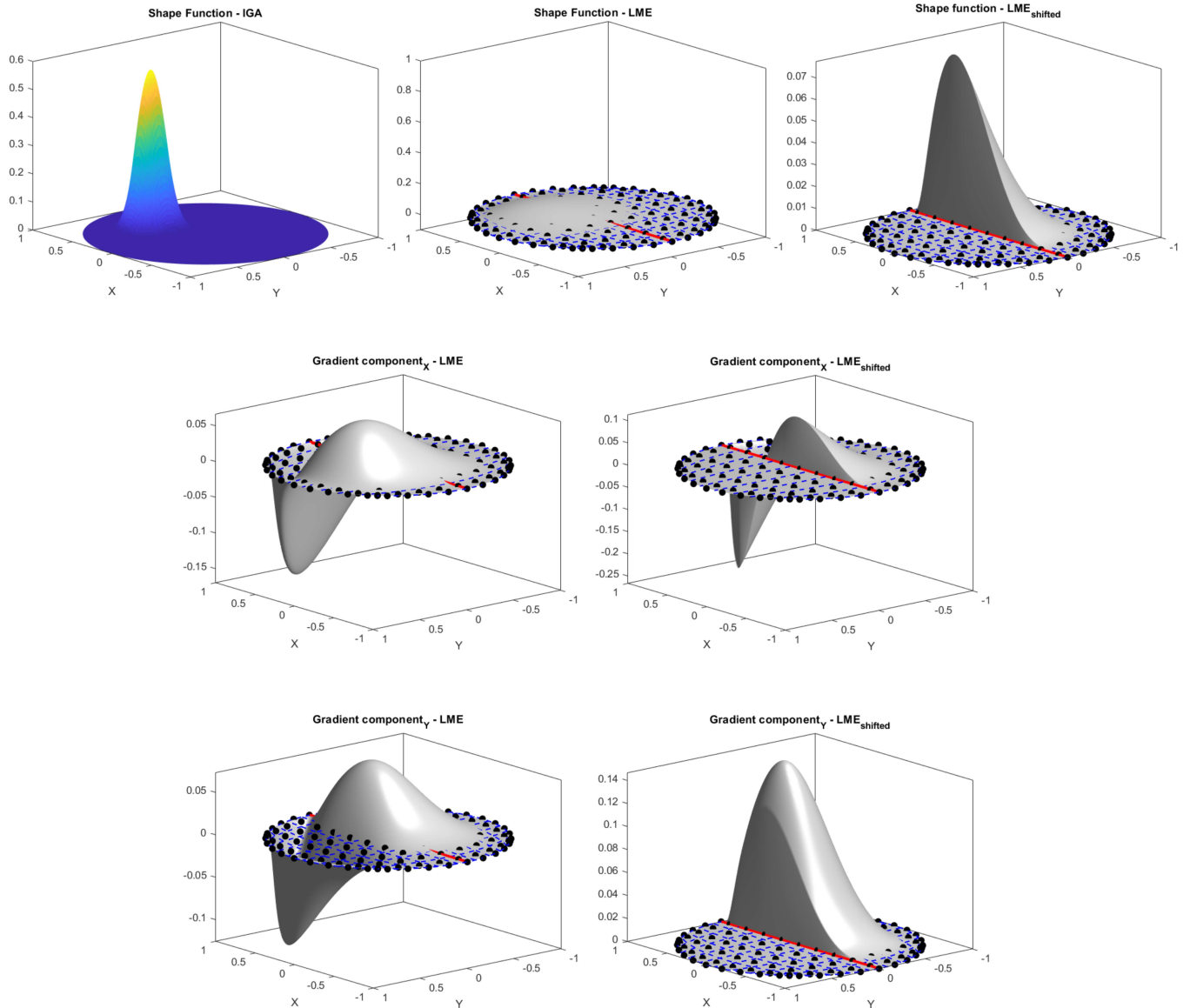
FIGURE 6 Shifting technique for the disk example with $\gamma = 0.1$. The top row at left represents the IGA basis function (coloured plot) for the standard section, while the LME values before and after shifting technique are shown in the middle and at the right, respectively. The gradients in the $\mathcal{X}$ and $\mathcal{Y}$-directions are given in the middle and the bottom rows before (left) and after (right) shifting.

TABLE 1 Radius of Gaussian decay of the basis function. The tolerance is set $\text{TOL}_0 = 10^{-8}$ for vanishing the support of the LME basis function.

γ	0.1	0.5	0.8	1	1.5	2
Λ	8.94	4	3.16	2.82	2.31	2
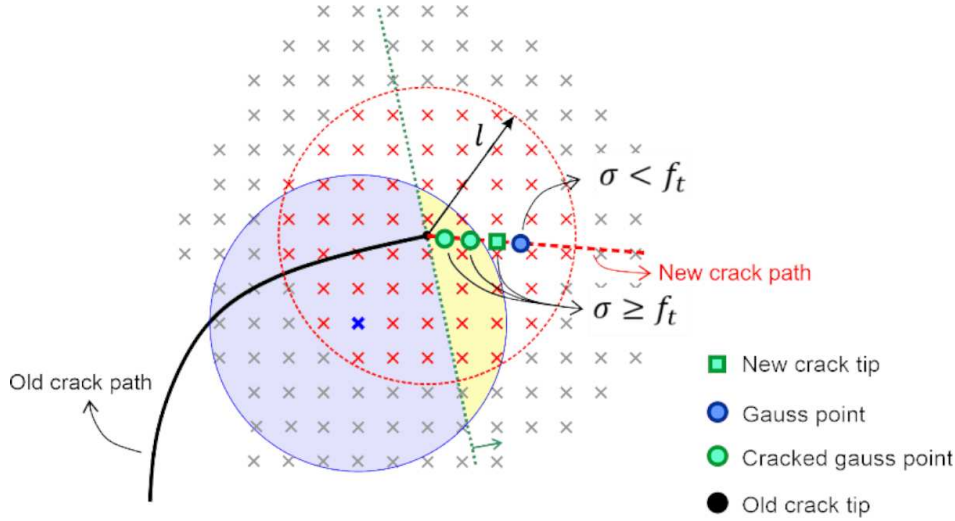
FIGURE 7 Crack extension determined with the non-local technique. The non-local approach involves the support of all points within the support of the old crack tip, i.e. all red crosses. As an example, the support of the blue cross is divided into two sections: the yellow part which denotes the intact material, i.e. where the Heaviside removes the effect of the discontinuity, and the purple part which indicates the area where both the standard and the enhanced fields exist.

4.2 | Compatibility enforcement

The shifting technique is adopted here as a means to enforce compatibility, Figure 3. This is new as shifting has not been used for a meshless approach within the extended framework. Furthermore, the blending technique with a Heaviside step function is exploited, an approach which effectively removes the discontinuous field in front of the crack tip[18], see the dashed red circle in Figure 4. This approach is robust, efficient and simple within the X-IGALME framework, definitely when compared to techniques to model cracks within a meshfree approach, such as the visibility or transparency criteria[36].

Employing shifting and blending, as well as Equations (7) and (11), the displacement field of Equation (5) becomes:

$$\mathbf{u}(\mathbf{x}) = \sum_{\mathcal{A} \in \mathcal{N}} \mathbf{R}_{\mathcal{A}}(\mathbf{x})\mathbf{a}_{\mathcal{A}} + \sum_{\mathcal{B} \in \mathcal{N}^{\mathcal{H}}} \mathcal{H}_{\Gamma_d}^{Bl}(\mathbf{x}) \left(\mathcal{H}_{\Gamma_d}^{GP}(\mathbf{x}) - \mathcal{H}_{\Gamma_d}^{B} \right) \mathbf{q}_{\mathcal{B}}(\mathbf{x})\mathbf{b}_{\mathcal{B}} \tag{23}$$

with $\mathcal{N}^{\mathcal{H}} \subset \mathcal{N}$ the subset enriched by the Heaviside function, while $\mathcal{H}_{\Gamma_d}^{B}$ and $\mathcal{H}_{\Gamma_d}^{GP}$ are the values of the Heaviside function at the control point $\mathcal{B}$ and the Gauss point under consideration defined by the sign function. $\mathcal{H}_{\Gamma_d}^{Bl}$ is the Heaviside function defined at the Gauss point with respect to the crack tip[18]. According to Equation (23) discretised equations are equipped with shifting and blending techniques at the discontinuity.

To demonstrate the effect of shifting, the basis function of an arbitrary point is illustrated for a disk, see Figure 5. Note that IGA accurately captures the curvature of the disk, and LME improves the accuracy of the enriched part. Figure 6 illustrates the effect of shifting on the basis functions in the first row. Shifted values of the gradients in the $\mathcal{X}$ and $\mathcal{Y}$-directions are compared with crude basis functions in the second and the third rows, respectively. Noteworthy is the fact that lower values for γ might help in enforcing the compatibility between the standard and the enhanced sections, i.e. in reducing the effect of the enhanced term at the location of control points.

4.3 | Direction of the crack extension

The higher-order continuity provided by IGA removes the stress jumps at element boundaries observed in the standard finite element analysis. Meshless techniques can provide an even higher accuracy, leading to a further improved estimate of the stresses around the crack tip. To determine the crack propagation direction, however, a more global estimate for stresses is required[18]. Thus, utilising a non-local like approach, an average of the stresses around the crack tip is used, thus estimating the crack propagation direction from averaged stress values, see Figure 7. Afterwards, the averaged local stress is compared with the fracture strength in the fracture criterion. The Gaussian distribution function[16,18] is utilised for the averaging. The same support width of the LME basis function is exploited as length scale, since it is normally larger than the length scale normally used in element-based approaches (2-3 times the length of the typical element[10]).
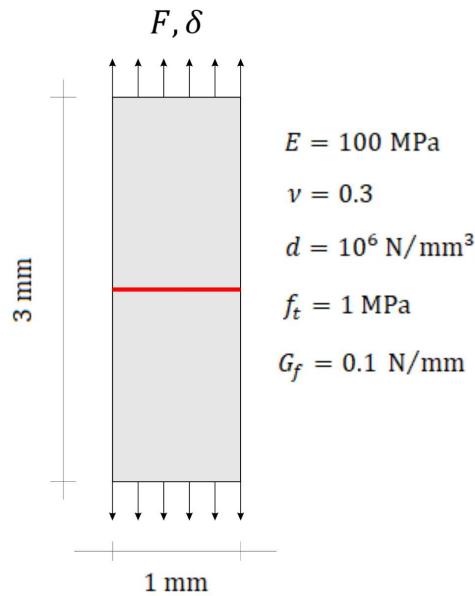
FIGURE 8 Geometry and material properties of a cracked plate (the crack is represented by the red solid line) subjected to simple tension. A dummy stiffness d is adopted to keep the interface element closed before the fracture criterion is met. F and δ denote the force and the displacement, respectively.

4.4 | Complementary features of IGA and LME

IGA and LME possess complementary features, allowing to mitigate the deficiencies of the other approach:

- The capability of IGA to model the geometry exactly mitigates the difficulty of LME to achieve sufficient accuracy at the boundary. On the other hand, LME improves the accuracy in the interior.

- When dealing with arbitrary crack paths, a disproportionate split of elements is inevitable in element-based extended approaches, which can lead to singularities[18,37]. Since a meshfree approach has been adopted for the enhanced part here, this issue is now eliminated. Therefore, any remeshing or node repositioning is unnecessary.

- Unlike XIGA[18] where two crack tips must be utilised – one for the enrichment scheme and another for the real location of the crack tip – just a single crack tip is now required. Accordingly, a simpler enrichment scheme can be adopted compared to the element-wise enrichment of XIGA.

- In contrast to XIGA, where different orders for the standard and extended parts are incompatible[17,18], LME and IGA can always be combined within X-IGALME, provided that the right combination of the node-set and the dimensionless aspect ratio γ have been chosen. Moreover, a super-quadratic convergence rate can then be obtained.
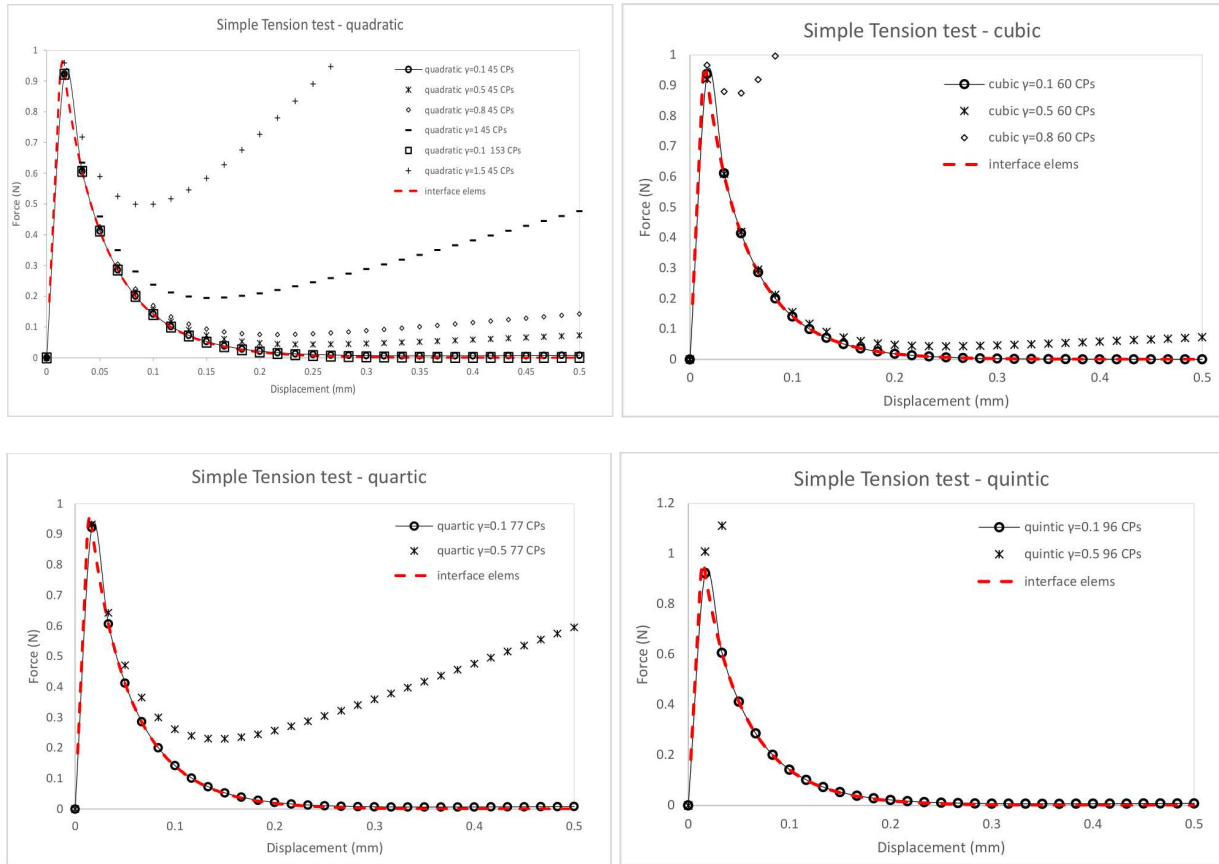
FIGURE 9 Load-displacement curve for the simple tension test. "CPs" denotes control points. "quartic", "cubic" and "quintic" denote the order of the NURBS.

5 | NUMERICAL EXAMPLES AND DISCUSSION

Now, the efficacy of the method is investigated at the hand of some numerical examples.

5.1 | NURBS order: simple tension test

In the first example the effect of different node sets and the dimensionless aspect ratio γ are assessed. The results are compared with a solution obtained using standard interface elements, where a dummy stiffness has been utilised to constrain the interface until the fracture criterion has been met. The geometry and the material properties are shown in Figure 8.

The results in Figure 9 indicate convergence for lower values of the dimensionless aspect ratio γ. This is shown for different NURBS orders for the standard part, leading to different node-sets for the enhanced part. It is noted that the same number of elements have been employed in the simulations to enable a proper comparison. For this case $\gamma = 0.1$ renders the best result for all NURBS orders.

To represent the differences between the NURBS orders utilised in this example, a log-log scale figure is plotted for the force-displacement curve resulted by $\gamma = 0.1$. A better performance in the form of a convergence trend is observed with the increase of the NURBS continuity-order (see Figure 10). Next is the effect of mesh refinement which is respectively compared with XIGA of the same order and linear XFEM, see Figure 11. The relative error is computed on the integral below the force-displacement curve $\int_0^\infty F \cdot \delta \, d\delta$, i.e. the error calculated on the dissipated energy. Results show a better performance of X-IGALME compared to XIGA and XFEM, except for the coarsest mesh of the quadratic order. Error patterns for X-IGALME, however, are not similar to each other or to XIGA, which is believed to be due to the meshfree characteristic of the extended part.
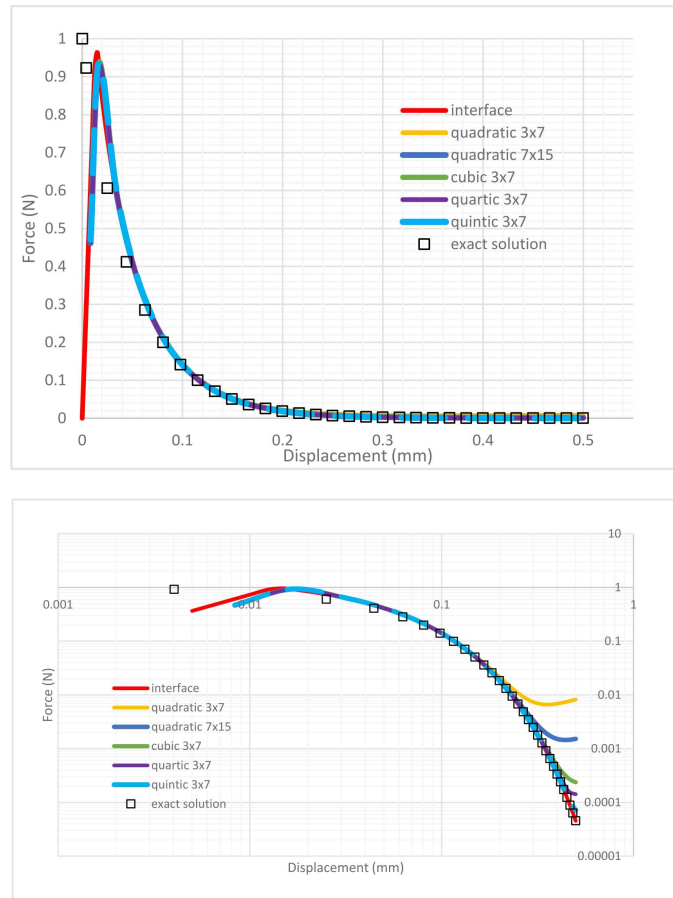
FIGURE 10 Force-displacement curves for $\gamma = 0.1$ are plotted for different NURBS orders, see the top. The logarithmic scale for both axes are plotted at the bottom. The numbers denote the number of elements in the $\mathcal{X}$ and $\mathcal{Y}$-directions respectively.
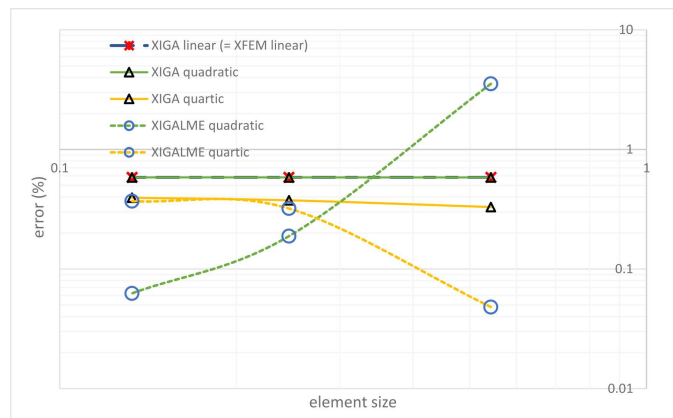
FIGURE 11 Relative error for the mesh refinement.

5.2 | Sensitivity analysis of singularity: simple tension test

A sensitivity analysis has been adopted to check the singularity of X-IGALME's stiffness matrix. This is important in the sense that element-wise approaches are known for this characteristic when the crack approaches one of the edges of the cracked element[37]. Therefore, a special enrichment is needed when the crack path coincides with the element edge in such approaches.
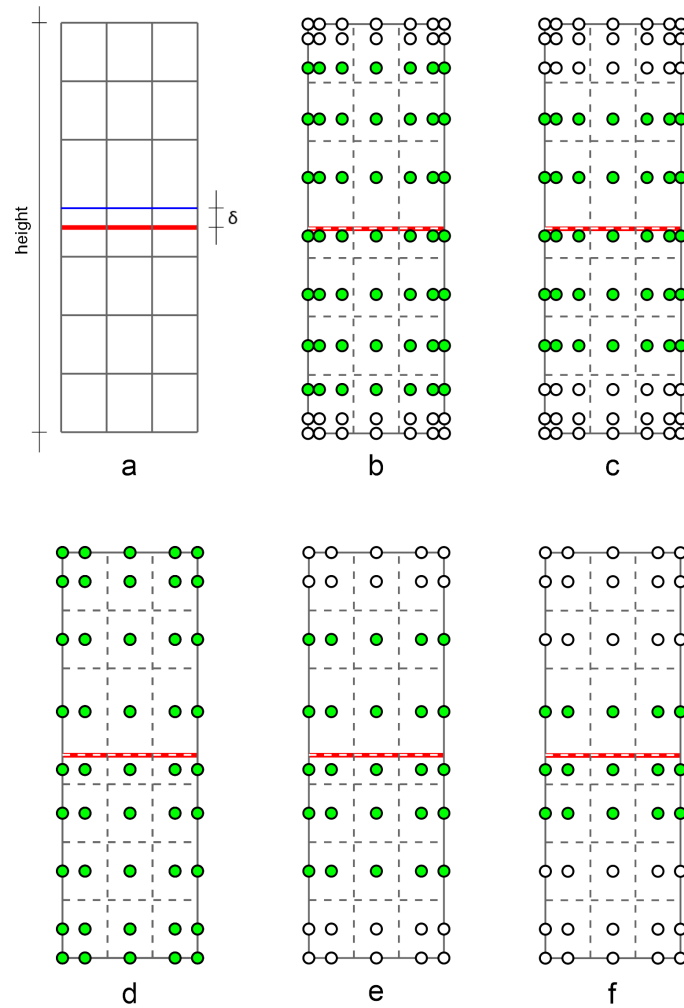
FIGURE 12 Sensitivity analysis for the singularity of X-IGALME. (a) defines the distance of the crack from the specified edge (the blue edge). Different cases of enrichment are shown for the coincidence of the crack and the specified edge: (b) and (c) are the normal and XIGA-like enrichment for X-IGALME in quartic order; (d), (e) and (f) denote the normal, the other enrichment and the XIGA-like enrichment for X-IGALME in quadratic order. X-IGALME is compared to XIGA and XFEM for different continuity-orders of NURBS.

The geometry is illustrated in Figure 12 which is similar to Section 5.1 with different enrichment cases when the crack coincides with the edge.

The results are presented in Figure 13. X-IGALME renders a stable trend even when the crack coincides with the edge. On the contrary, the other approaches return very high condition numbers for the stiffness matrices which implies an instability of the solution. The condition number for X-IGALME becomes even more stable when less control points are enriched, e.g. where the enrichment meets XIGA enrichment. This shows the stability of the solution. Nevertheless, the stability of X-IGALME provides a single prescription of the enrichment (see Figures 14.a and 14.c), while a special enrichment for element-wise approaches is needed where the crack coincides with the edge of the cracked element (see Figure 14.b), otherwise singularity results.

To assess the accuracy of the solution by the condition numbers reported in Figure 13, the area below the force displacement curve is calculated for quartic order and is compared to quartic XIGA, see Figure 15. Generally, errors are below 1%. X-IGALME with the XIGA-like enrichment shows the best performance at the smallest distances of the crack from the edge. This deteriorates further away (bigger δ values), where the normal enrichment of X-IGALME is superior. Noteworthy is the fact that XIGA and XIGA-like enrichment for X-IGALME render close results.
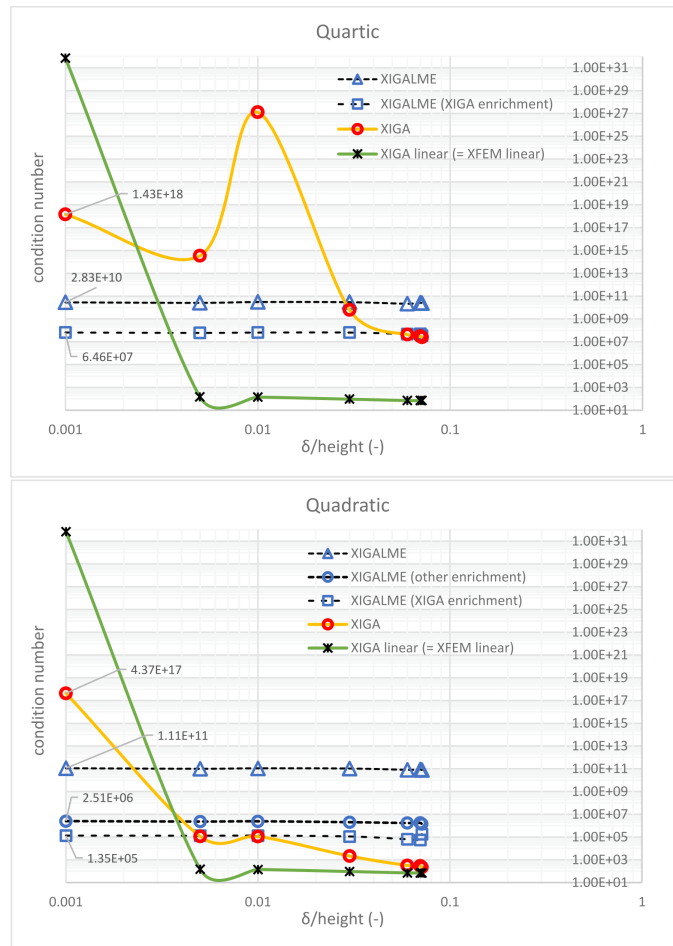
FIGURE 13 Condition number comparison of XIGALME with XIGA and linear XFEM.

TABLE 2 Integration of load-displacement curves (dissipated energy).

Case	Qd†-0.3-1062‡	Qd-0.5-1062	Qd-0.8-1062	Qr-0.3-1062	Qr-0.5-1062	Qr-0.8-1062	Qr-0.3-702
Area(Nmm)	0.3212	0.4172	0.5803	0.2959	0.3120	0.3296	0.3079

†Qd: quadratic NURBS; Qr: quartic NURBS.

‡The order follows *type-γ-elems*; e.g. Qd-0.5-1062 denotes quadratic - $\gamma = 0.5$ - 1062 elements.

5.3 | Aspect ratio effect on energy dissipation: Three Point Bending test

The effect of the dimensionless aspect ratio γ on the energy dissipation have been investigated for a Three Point Bending (TPB) test. The geometry and the material properties are shown in Figure 16. As noted before, the shear stiffness has been set equal to zero in order to obtain a symmetric stiffness matrix. To investigate whether the energy dissipation is independent of the spatial discretisation, the dissipated energy is compared with the fracture energy, 0.3 Nmm. From the results in Table 2 we conclude that lower γ values lead to a convergence towards the case of $\gamma = 0.3$, see Figure 16. In addition, the dissipated energy for $\gamma = 0.3$ is closer to the fracture energy, supporting the conclusion made in Section 5.1, namely that lower values for γ yield better results. From the perspective of the NURBS order, the results for the quadratic discretisation are acceptable only when $\gamma = 0.3$. For a quartic NURBS, however, all γ values yield satisfactory results, although the trend holds that better results are obtained for lower values of γ. To study the effect of the spatial discretisation, a coarse quartic NURBS mesh has been examined with $\gamma = 0.3$. The results for the coarse and fine meshes appear to coincide.
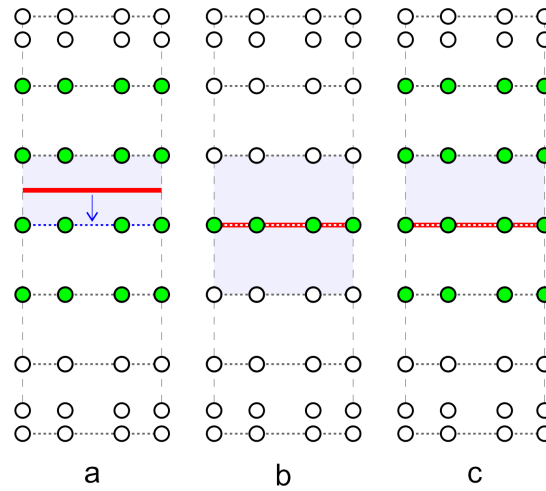
FIGURE 14 Enrichment prescriptions for X-IGALME and other element-wise extended approaches. A cubic order has been adopted for discretisation and the shade indicates the cracked element/elements. (a) indicates the crack inside the element whose enrichment is the same for X-IGALME and other approaches. Locating the crack on the blue edge necessitates a special enrichment shown in (b) for element-wise extended approaches. For X-IGALME, however, the same enrichment as (a) can be preserved, c.f. (c).
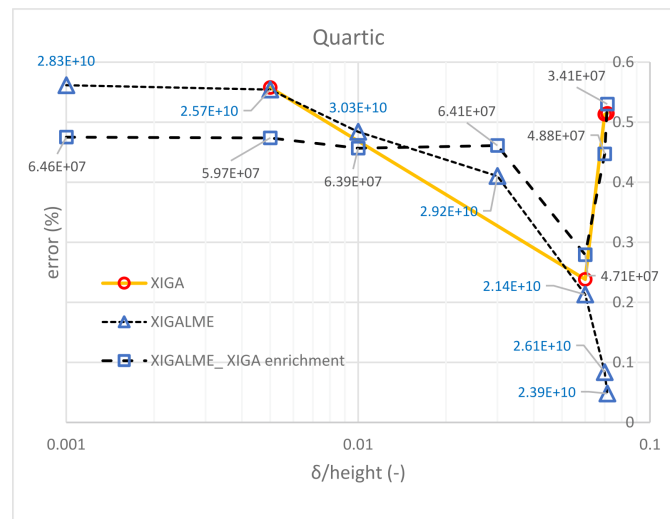
FIGURE 15 Error estimation of the singularity analysis (see Figure 13) for quartic order. The digits correspond to the condition number of each case. XIGA is only reported for stable cases.

5.4 | Straight crack propagation: peeling test

A Double Cantilever Beam (DCB), shown in Figure 18, is now investigated. Different from the TPB test, the significance of this example lies in the propagation which takes place perpendicular to the smaller edge of the beam, where the node set plays a crucial role for the enhanced part. The material properties are as follows: The Young's modulus, Poisson's ratio, the tensile strength and the fracture energy are $E = 100$ MPa, $\nu = 0.3$, $f_t = 1$ MPa and $G_f = 0.1$ Nmm^{-1}, respectively. For the interface elements, which serve as the benchmark, the dummy stiffness $d = 10^6$ Nmm^{-3} to prevent negative openings. The results are also compared with findings from XIGA[18].

As expected, the results are unstable or divergent for coarse meshes in the vertical direction. While maintaining the same mesh in the horizontal direction, a mesh refinement in the vertical direction leads to a failure of the line-search technique to
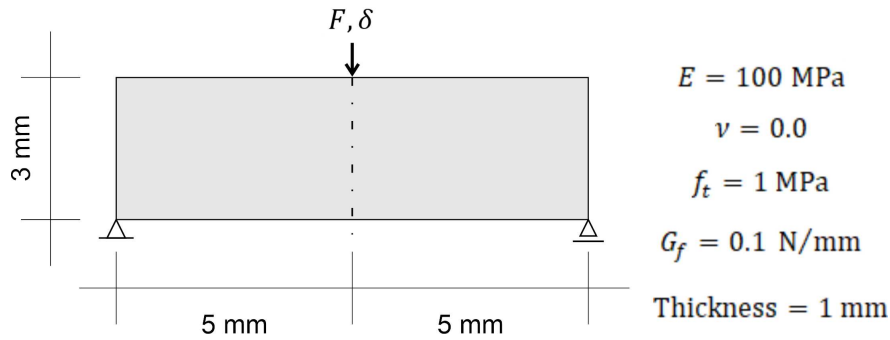
FIGURE 16 Geometry and material properties of Three Point Bending test.
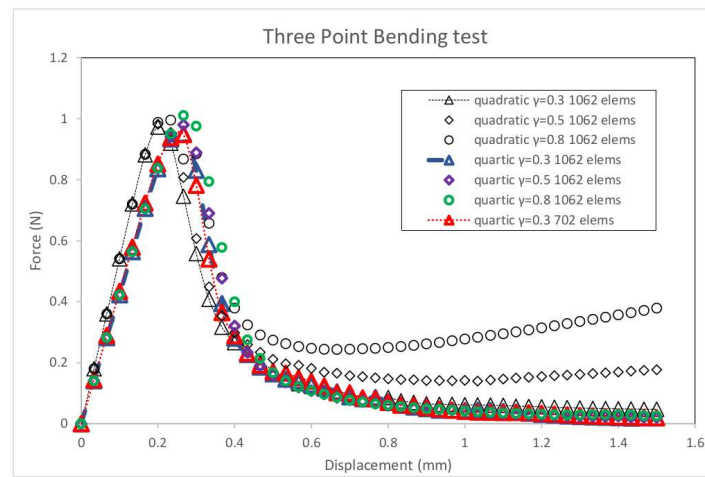
FIGURE 17 Load-displacement curves for the Three Point Bending test using different γ-values. Quadratic and quartic denote the order of the NURBS.

compute the LME basis function [20,22]. Hence, a uniform nodal spacing is used, which facilitates LME procedure and improves the crack propagation. This leads to a finer mesh compared to XIGA [18], see the blue triangles in Figure 19.a.

The values for γ are problem-dependent (node set-specific). It can be improved by optimising the value for γ at each point. This optimisation problem can be solved by adopting a variational approach which considers the physical field as well as the locality of the basis functions [25].

For cohesive fracture, the moment of crack propagation is central in obtaining a smooth mechanical response. Although cohesive fracture is energy-based, i.e. it compensates a belated fracture initiation in forthcoming loading steps, a jagged response can be inevitable. The results presented here are obtained for a stress-based fracture criterion, i.e. $\sigma_y^{loc} \geq f_t$. To investigate the effect of the fracture criterion on the jagged response of Figure 19.a (blue triangles), we have adopted the additional criterion of a positive displacement jump, similar to the criterion used in interface elements. However, while the degrees of freedom are uniquely defined for an interface element and a dummy stiffness guarantees the non-negativity of the displacement jump, this requires more effort for an extended method, since a fictitious crack propagation with new degrees of freedom must be defined. Afterwards, a new nested solution is necessary for the new, temporary configuration to compute the displacement jumps. The extension will become permanent upon satisfaction of the displacement fracture criterion. Otherwise, the previous configuration of crack is used. The same number of elements and the same NURBS order are used (similar to the blue triangles in Figure 19.a). This results in Figure 19.b, where there is less noise (lower amplitude) for the present approach. The results are also compared with those from XIGA. A further refinement is utilised to obtain the smoothest solution, see the dashed black line in Figure
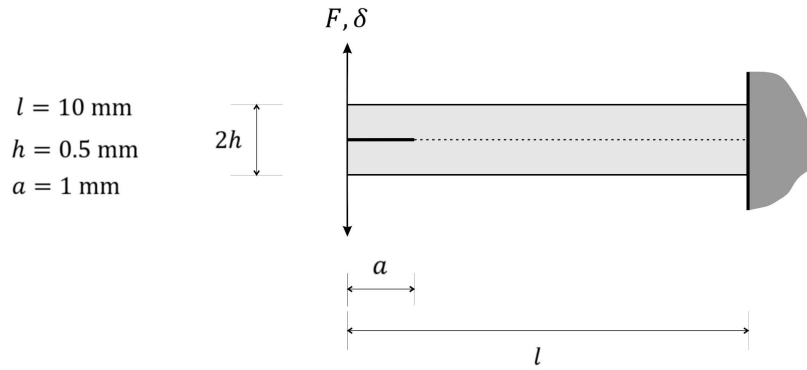
FIGURE 18 Double Cantilever Beam with an initial notch subjected to mode-I loading.

19.c. X-IGALME's best results are compared with interface element and XFEM approaches, in Figure 19.c. The corresponding relative errors (based on the integral below the force-displacement curves) are plotted in Figure 19.d. The smallest error is observed for the interface element showing closer response of X-IGALME to this approach, while the mean error (mean of the interface element and XFEM errors) is around two percent. The peak values of X-IGALME are also closer to the interface element approach, except for the $\gamma = 0.5$ which is closer to XFEM.

5.5 | Arbitrary crack propagation: TPB test with eccentric crack

Free crack propagation is now examined within a TPB test similar to that in Section 5.3. The key difference is that now the crack is forced to initiate 0.7 millimeters away from the centreline (see Figure 20). Therefore, an eccentric propagation is promoted with a curved crack profile is the result. The material properties are given in Figure 20, and $\gamma = 0.3$ for the quadratic and the quartic discretisations in conformity with the results of Section 5.3. Figure 21 gives the crack paths, which are compared with that which results from XFEM[38]. The results almost coincide.

5.6 | Exact parametrisation of a curved geometry: circular plate with multiple holes

A circular plate with a slit in the centre is subjected to prescribed displacements at the boundary to evaluate X-IGALME in an exact parametrisation of a curved geometry. The performance in the presence of multiple holes is also investigated by 6 holes comprised of 2 different sizes. Geometry and discretisation/node-set are presented in Figure 22. The crack length is 0.4 mm and the radii for the disk, C1 and C2 holes are 1, 0.1 and 0.2 millimeters, respectively. Void level set has been adopted for modelling the holes, where unlike element-wise extended approaches, no special care has to be exercised in enrichment[18] due to the singularity-free characteristic of the X-IGALME. The material properties are given as: $E = 100$ MPa; $v = 0$; $G_f = 0.1$ N/mm; $\gamma = 1$ and $f_t = 1$ MPa. The slit and the fracturing are set traction-free.

The solution is first benchmarked against XIGA without any hole for the full propagation of the crack through the entire disk. In a second analysis only C1 holes are considered where the stiffness is lower than the first case (the blue line with rectangles is below the yellow/red line). The location of C1 holes delays the propagation of the initial slit. Adding C2 holes to the problem significantly reduces the stiffness (the green line with triangles is blow the others). A softening phenomenon happens once again upon crack propagation until it reaches the C2 holes. Afterwards, a delay in propagation of the crack (due to the presence of C2 holes) renders a hardening behavior followed by alternate softening responses.

6 | CONCLUDING REMARKS

Isogeometric analysis has been augmented with local maximum entropy in an extended framework, which has been coined X-IGALME. The high accuracy of isogeometric analysis in capturing complex boundaries together with the high accuracy of the local maximum entropy approach in the interior renders the method an excellent alternative within the class of extended
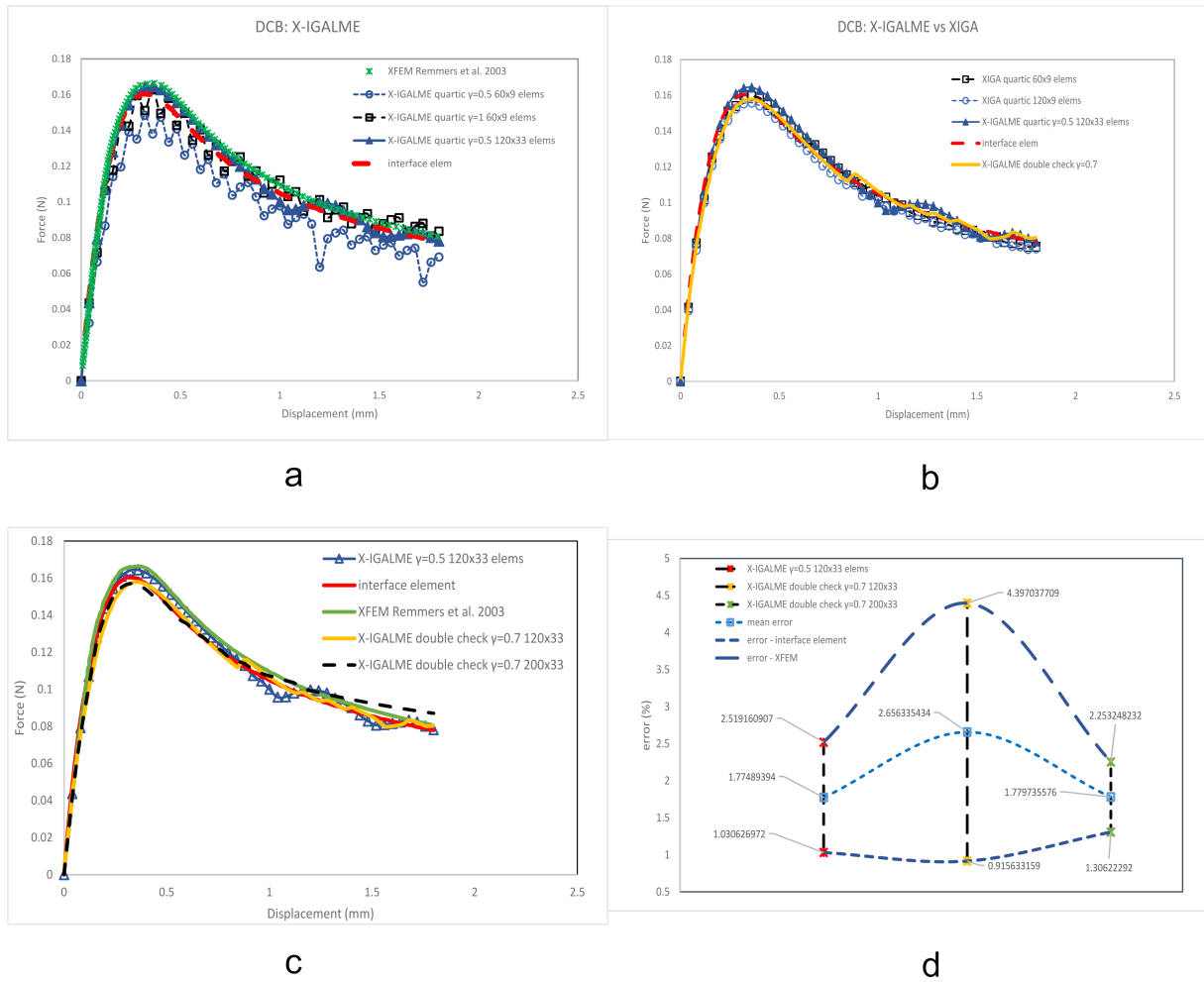
FIGURE 19 Load-displacement curve for the Double Cantilever Beam. The results are compared with interface elements and XFEM[11] in (a) and (c), while a comparison between X-IGALME and XIGA has been made in (b). The numbers in the legend denote the number of elements in the $\mathcal{X}$ and in the $\mathcal{Y}$-directions, respectively. The best results of X-IGALME are compared with Interface element and XFEM in (c). The relative error (integral under the curve) is plotted for X-IGALME results benchmarked against interface element and XFEM approaches in (d).

discretisation methods. The higher continuity-order provided by both IGA and LME leads to an improved estimate of stresses which is central in finding the correct crack extension direction. Moreover, it sets the scene for higher-order differential equations.

The approach has been assessed for different NURBS orders, node sets and values of the aspect ratio γ. It is proven that the choice for γ is node-set specific. Nevertheless, despite failing to return the conventional error pattern for mesh refinement, the errors show a better performance for X-IGALME in almost all cases. It has been observed that lower values for γ return correct results. This is in line with the hypothesis that the lower values of γ help in compatibility enforcement. The effect of γ on the energy dissipation has been investigated as well, supporting the conclusion about the lower values of γ. An optimisation problem on how to choose the value of γ for a given node-set is a potential topic for a future research. The role of different quadrature rules on the solution is another topic to explore.

A detailed sensitivity analysis of singularity has been performed on X-IGALME. The results indicate a guaranteed stability of the solution for X-IGALME, where XIGA and XFEM fail. Unlike element-wise approaches, the singularity-free characteristic of X-IGALME facilitates a single prescription for enrichment in any condition, including void level set. Finally, straight and curved fractures as well as voids have been simulated successfully for straight and curved geometries. Indeed, X-IGALME possesses some excellent features as a result from combining of an isogeometric finite element scheme and a meshless technique.
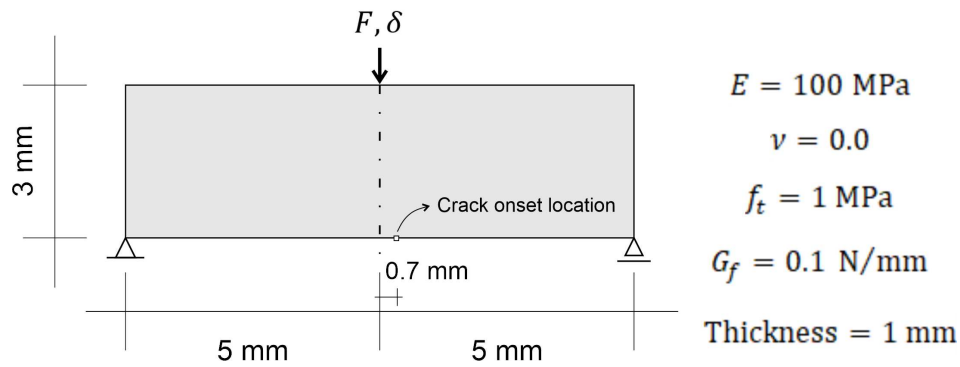
FIGURE 20 Three-Point Bending test with an eccentric crack.
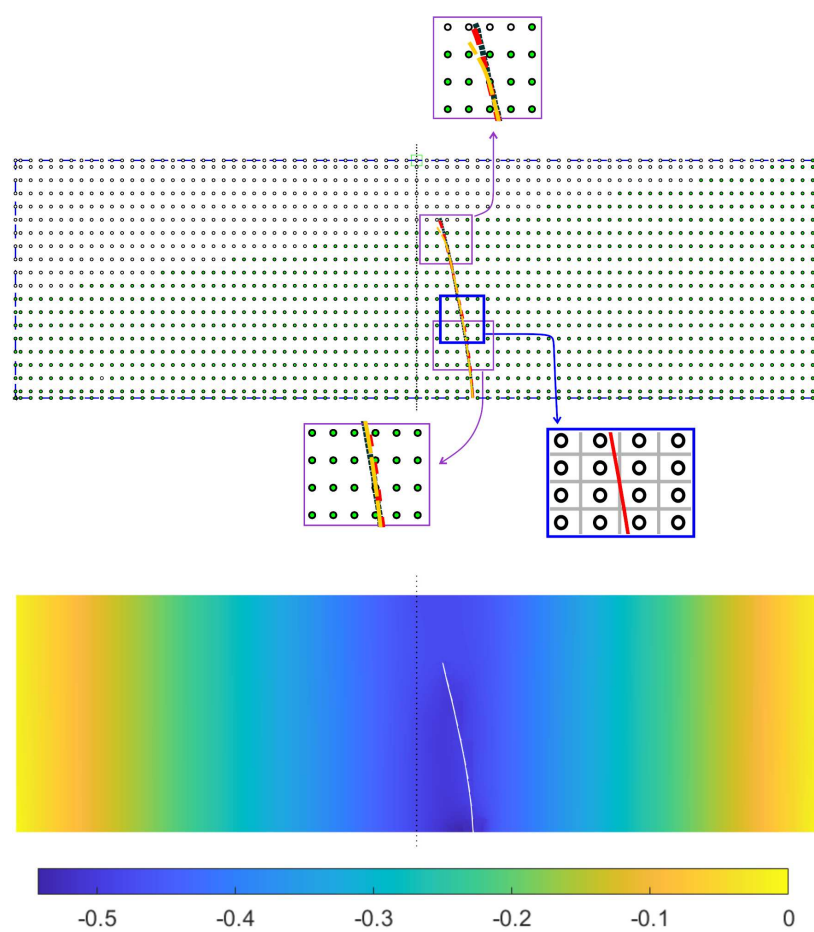
FIGURE 21 Crack profiles for the quadratic (solid red line) and the quartic NURBS (dashed yellow line). These results are compared with XFEM [38] (dotted black line). The displacement contour in the $\mathcal{Y}$-direction is given for the quadratic discretisation. The values of the colour bar are given in millimeters.

ACKNOWLEDGMENTS
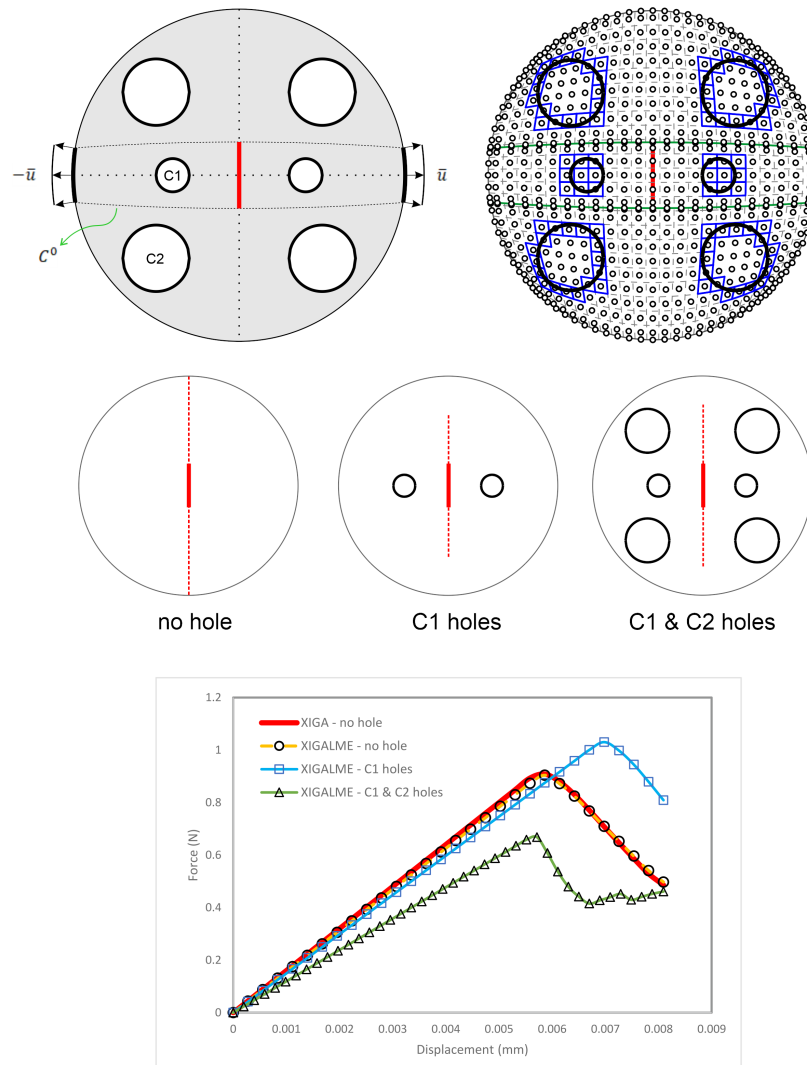
FIGURE 22 A disk with an initial slit and multiple holes is presented. Crack propagation is investigated for three cases: no hole; C1 holes; C1 and C2 holes. Force-displacement curves are also plotted for the three cases and are compared to XIGA for the no hole case.

DATA AVAILABILITY STATEMENT

Data sharing is not applicable to this article as no datasets were generated or analysed during this study.

CONFLICT OF INTEREST

The authors declare that there is no conflict of interest regarding the publication of this paper.

How to cite this article: Fathi F., Chen L., and de Borst R. (2020), X-IGALME: An isogeometric analysis augmented with local maximum entropy for cohesive fracture, *Int J Numer Methods Eng.*, *2021*.

APPENDIX

A DERIVATIVES OF THE LME BASIS FUNCTIONS

We define the functions [22,25,39]:

$$f_a(\mathbf{x}, \lambda, \beta_a) = -\beta_a |\mathbf{x} - \mathbf{x}_a|^2 + \lambda \cdot (\mathbf{x} - \mathbf{x}_a), \tag{A1}$$

$$q_a(\mathbf{x}, \lambda, \boldsymbol{\beta}) = \frac{\exp[f_a(\mathbf{x}, \lambda, \beta_a)]}{Z(\mathbf{x}, \lambda, \boldsymbol{\beta})}, \tag{A2}$$

where $Z(\mathbf{x}, \lambda, \boldsymbol{\beta}) = \sum_b \exp[f_b(\mathbf{x}, \lambda, \beta_b)]$ and

$$\mathbf{r}(\mathbf{x}, \lambda, \boldsymbol{\beta}) = \sum_a q_a(\mathbf{x}, \lambda, \boldsymbol{\beta})(\mathbf{x} - \mathbf{x}_a), \tag{A3}$$

$$\mathbf{J}(\mathbf{x}, \lambda, \boldsymbol{\beta}) = \frac{\partial \mathbf{r}}{\partial \lambda} = \sum_a q_a(\mathbf{x}, \lambda, \boldsymbol{\beta})(\mathbf{x} - \mathbf{x}_a) \otimes (\mathbf{x} - \mathbf{x}_a) - \mathbf{r}(\mathbf{x}, \lambda, \boldsymbol{\beta}) \otimes \mathbf{r}(\mathbf{x}, \lambda, \boldsymbol{\beta}) \tag{A4}$$

with a and b denoting the nodes. Recalling Equation 16, the superscript $*$ explicitly and implicitly relates the value of $\mathbf{x}$ and $\boldsymbol{\beta}$ [25]. Accordingly, any value within this superscript follows Equation 16 and falls into this dependency. It is noted that the LME basis function in Equation 14 is now denoted by q^*. The first and second spatial derivatives (which equals the Hessian $\mathbb{H}$) read [39]:

$$\nabla q_a^* = q_a^*(\mathbf{r}_\beta - \mathbf{M}_a(\mathbf{x} - \mathbf{x}_a)) \tag{A5}$$

and

$$\begin{aligned}
\mathbb{H}q_a^* = q_a^* \left(\mathbf{r}_\beta - \mathbf{M}_a(\mathbf{x} - \mathbf{x}_a)\right) \otimes \left(\mathbf{r}_\beta - \mathbf{M}_a(\mathbf{x} - \mathbf{x}_a)\right) + 2q_a^* \left(\sum_b \beta_b q_b^* - \beta_a\right)\mathbf{1} \\
+ q_a^* \left(\mathbf{r}_\beta \otimes \mathbf{r}_\beta + \mathbf{r}_\beta \otimes \mathbf{j}_a + \mathbf{j}_a \otimes \mathbf{r}_\beta + (\mathbf{r}_\beta \cdot \mathbf{j}_a)\mathbf{1}\right) \\
- q_a^* \sum_b q_b^*(1 + \Delta_{ab})\mathbf{M}_b(\mathbf{x} - \mathbf{x}_b) \otimes \mathbf{M}_b(\mathbf{x} - \mathbf{x}_b)
\end{aligned} \tag{A6}$$

where

$$\mathbf{r}_\beta = 2 \sum_a \beta_a q_a^*(\mathbf{x} - \mathbf{x}_a), \tag{A7}$$

$$\mathbf{j}_a = (\mathbf{J}^*)^{-1}(\mathbf{x} - \mathbf{x}_a), \tag{A8}$$

$$\Delta_{ab} = (\mathbf{x} - \mathbf{x}_b) \cdot (\mathbf{J}^*)^{-1}(\mathbf{x} - \mathbf{x}_a), \tag{A9}$$

$$\mathbf{M}_a = 2\beta_a \mathbf{1} - (\mathbf{J}_\beta - \mathbf{1})(\mathbf{J}^*)^{-1} \tag{A10}$$

while $\mathbf{1}$ indicates the identity matrix and

$$\mathbf{J}_\beta = 2 \sum_a \beta_a q_a^*(\mathbf{x} - \mathbf{x}_a) \otimes (\mathbf{x} - \mathbf{x}_a). \tag{A11}$$

References

1. Schellekens JCJ, de Borst R. On the numerical integration of interface elements. *International Journal for Numerical Methods in Engineering* 1993; 36: 43–66.

2. Irzal F, Remmers JJC, Verhoosel CV, de Borst R. An isogeometric analysis Bézier interface element for mechanical and poromechanical fracture problems. *International Journal for Numerical Methods in Engineering* 2014; 97: 608–628.

3. Vignollet J, May S, de Borst R. On the numerical integration of isogeometric interface elements. *International Journal for Numerical Methods in Engineering* 2015; 102: 1773–1749.

4. Chen L, Lingen EJ, de Borst R. Adaptive hierarchical refinement of NURBS in cohesive fracture analysis. *International Journal for Numerical Methods in Engineering* 2017; 112: 2151–2173.

5. Ingraffea AR, Saouma V. Numerical modelling of discrete crack propagation in reinforced and plain concrete. In: Dordrecht: Martinus Nijhoff Publishers. 1985 (pp. 171–225).

6. Secchi S, Simoni L, Schrefler BA. Mesh adaptation and transfer schemes for discrete fracture propagation in porous materials. *International Journal for Numerical and Analytical Methods in Geomechanics* 2007; 31: 331–345.

7. Belytschko T, Black T. Elastic crack growth in finite elements with minimal remeshing. *International Journal for Numerical Methods in Engineering* 1999; 45: 601–620.

8. Moës N, Dolbow J, Belytschko T. A finite element method for crack growth without remeshing. *International Journal for Numerical Methods in Engineering* 1999; 46: 131–150.

9. Fries TP, Belytschko T. The extended/generalized finite element method: An overview of the method and its applications. *International Journal for Numerical Methods in Engineering* 2010; 84: 253–304.

10. Wells GN, Sluys LJ. A new method for modelling cohesive cracks using finite elements. *International Journal for Numerical Methods in Engineering* 2001; 50: 2667–2682.

11. Remmers JJC, de Borst R, Needleman A. A cohesive segments method for the simulation of crack growth. *Computational Mechanics* 2003; 31: 69–77.

12. Cottrell JA, Hughes TJR, Bazilevs Y. *Isogeometric Analysis: Toward Integration of CAD and FEA*. Chichester: John Wiley & Sons . 2009.

13. Verhoosel CV, Scott MA, de Borst R, Hughes TJR. An isogeometric analysis approach to cohesive zone modelling. *International Journal for Numerical Methods in Engineering* 2011; 87: 336–360.

14. Chen L, Verhoosel CV, de Borst R. Discrete fracture analysis using locally refined T-splines. *International Journal for Numerical Methods in Engineering* 2018; 116: 117–140.

15. May S, de Borst R, Vignollet J. Powell-Sabin B-splines for smeared and discrete approaches to fracture in quasi-brittle materials. *Computer Methods in Applied Mechanics and Engineering* 2016; 307: 193–214.

16. Chen L, de Borst R. Cohesive fracture analysis using Powell-Sabin B-splines. *International Journal for Numerical and Analytical Methods in Geomechanics* 2019; 43: 625–640.

17. De Luycker E, Benson DJ, Belytschko T, Bazilevs Y, Hsu MC. X-FEM in isogeometric analysis for linear fracture mechanics. *International Journal for Numerical Methods in Engineering* 2011; 87: 541–565.

18. Fathi F, Chen L, de Borst R. Extended isogeometric analysis for cohesive fracture. *International Journal for Numerical Methods in Engineering* 2020; 121: 4584–4613.

19. Fathi F, de Borst R. Geometrically nonlinear extended isogeometric analysis for cohesive fracture with applications to delamination in composites. *Finite Element in Analysis and Design* 2021.

20. Sukumar N. Construction of polygonal interpolants: a maximum entropy approach. *International Journal for Numerical Methods in Engineering* 2004; 61: 2159–2181.

21. Rosolen A, Arroyo M. Blending isogeometric analysis and local maximum entropy meshfree approximants. *Computer Methods in Applied Mechanics and Engineering* 2013; 264: 95–107.

22. Arroyo M, Ortiz M. Local maximum-entropy approximation schemes: a seamless bridge between finite elements and meshfree methods. *International Journal for Numerical Methods in Engineering* 2006; 65: 2167–2202.

23. Bompadre A, Perotti LE, Cyron CJ, Ortiz M. Convergent meshfree approximation schemes of arbitrary order and smoothness. *Computer Methods in Applied Mechanics and Engineering* 2012; 221: 83–103.

24. Rosolen A, Millán D, Arroyo M. Second-order convex maximum entropy approximants with applications to high-order PDE. *International Journal for Numerical Methods in Engineering* 2013; 94: 150–182.

25. Rosolen A, Millán D, Arroyo M. On the optimum support size in meshfree methods: a variational adaptivity approach with maximum-entropy approximants. *International Journal for Numerical Methods in Engineering* 2010; 82: 868–895.

26. Huerta A, Fernández-Méndez S. Enrichment and coupling of the finite element and meshless methods. *International Journal for Numerical Methods in Engineering* 2000; 48: 1615–1636.

27. Valizadeh N, Bazilevs Y, Chen JS, Rabczuk T. A coupled IGA-meshfree discretization of arbitrary order of accuracy and without global geometry parameterization. *Computer Methods in Applied Mechanics and Engineering* 2015; 293: 20–37.

28. Kumar S, Danas K, Kochmann DM. Enhanced local maximum-entropy approximation for stable meshfree simulations. *Computer Methods in Applied Mechanics and Engineering* 2019; 344: 858–886.

29. Amiri F, Anitescu C, Arroyo M, Bordas SPA, Rabczuk T. XLME interpolants, a seamless bridge between XFEM and enriched meshless methods. *Computational Mechanics* 2014; 53(1): 45–57.

30. Khoei AR. *Extended finite element method: theory and applications*. John Wiley & Sons . 2014.

31. Gómez H, Calo VM, Bazilevs Y, Hughes TJR. Isogeometric analysis of the Cahn–Hilliard phase-field model. *Computer methods in applied mechanics and engineering* 2008; 197: 4333–4352.

32. Kästner M, Metsch P, de Borst R. Isogeometric analysis of the Cahn-Hilliard equation–a convergence study. *Journal of Computational Physics* 2016; 305: 360–371.

33. de Borst R, Crisfield MA, Remmers JJ, Verhoosel CV. *Nonlinear Finite Element Analysis of Solids and Structures*. Chichester: John Wiley & Sons. 2nd ed. 2012.

34. Borden MJ, Scott MA, Evans JA, Hughes TJR. Isogeometric finite element data structures based on Bézier extraction of NURBS. *International Journal for Numerical Methods in Engineering* 2011; 87: 15–47.

35. de Borst R, Chen L. The role of Bézier extraction in adaptive isogeometric analysis: Local refinement and hierarchical refinement. *International Journal for Numerical Methods in Engineering* 2018; 113: 999–1019.

36. Organ D, Fleming M, Terry T, Belytschko T. Continuous meshless approximations for nonconvex bodies by diffraction and transparency. *Computational Mechanics* 1996; 18: 225–235.

37. Zhang Q, Babuška I, Banerjee U. Robustness in stable generalized finite element methods (SGFEM) applied to Poisson problems with crack singularities. *Computer Methods in Applied Mechanics and Engineering* 2016; 311: 476–502.

38. Askes H, Wells GN, de Borst R. Novel discretization concepts. In: de Borst R, Mang HA., eds. *Comprehensive Structural Integrity*. Volume 3: Numerical and Computational Methods. Oxford: Elsevier. 2003 (pp. 377–425).

39. Millán D, Rosolen A, Arroyo M. Thin shell analysis from scattered points with maximum-entropy approximants. *International Journal for Numerical Methods in Engineering* 2011; 85: 723–751.